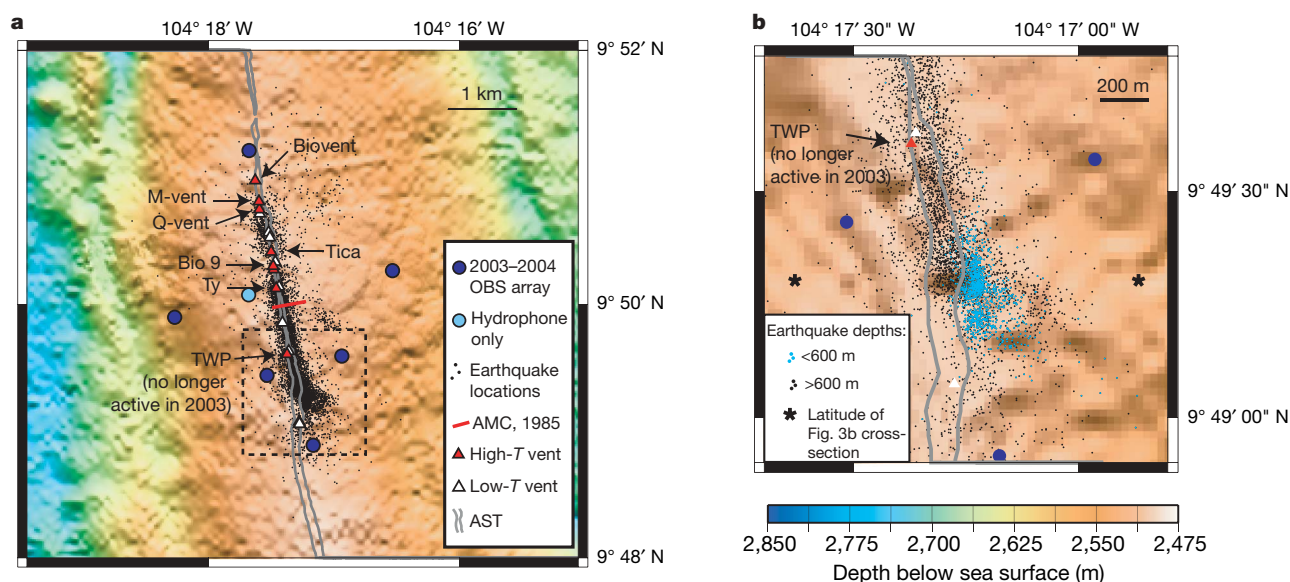# LETTERS

Seismic identification of along-axis hydrothermal flow on the East Pacific Rise

M. Tolstoy[1], F. Waldhauser[1], D. R. Bohnenstiehl[1]†, R. T. Weekly[1] & W.-Y. Kim[1]

Hydrothermal circulation at the axis of mid-ocean ridges affects the chemistry of the lithosphere and overlying ocean, supports chemosynthetic biological communities and is responsible for significant heat transfer from the lithosphere to the ocean[1–3]. It is commonly thought that flow in these systems is oriented across the ridge axis, with recharge occurring along off-axis faults[4–6], but the structure and scale of hydrothermal systems are usually inferred from thermal and geochemical models constrained by the geophysical setting[7–9], rather than direct observations. The presence of microearthquakes may shed light on hydrothermal pathways by revealing zones of thermal cracking where cold sea water extracts heat from hot crustal rocks, as well as regions where magmatic and tectonic stresses create fractures that increase porosity and permeability. Here we show that hypocentres beneath a well-studied hydrothermal vent field on the East Pacific Rise cluster in a vertical pipe-like zone near a small axial discontinuity, and in a band that lies directly above the axial magma chamber. The location of the shallow pipe-like cluster relative to the distribution and temperature of hydrothermal vents along this section of the ridge suggests that hydrothermal recharge may be concentrated there as a

consequence of the permeability generated by tectonic fracturing. Furthermore, we interpret the band of seismicity above the magma chamber as a zone of hydrothermal cracking, which suggests that hydrothermal circulation may be strongly aligned along the ridge axis. We conclude that models that suggest that hydrothermal cells are oriented across-axis, with diffuse off-axis recharge zones, may not apply to the fast-spreading East Pacific Rise.

The mass and energy transfer produced by hydrothermal circulation at the mid-ocean-ridge axis has been studied widely since deep-sea hydrothermal vent systems were discovered[10] in 1977. The location of seawater recharge has been particularly elusive: although it is most commonly inferred to be along off-axis faults[4–6], it also has been proposed that down-flow may occur on-axis[6,11,12]. One of the best-studied mid-ocean-ridge vent fields is at 9° 50′ N on the East Pacific Rise (EPR), where detailed biological, chemical, geophysical and geological studies have monitored and characterized this site for more than 15 years. Indeed, a full volcanic cycle has now been observed with a 1991–92 eruption[13,14] paved over by a 2006 eruption following more than a 2-yr build-up in seismicity rate[15].
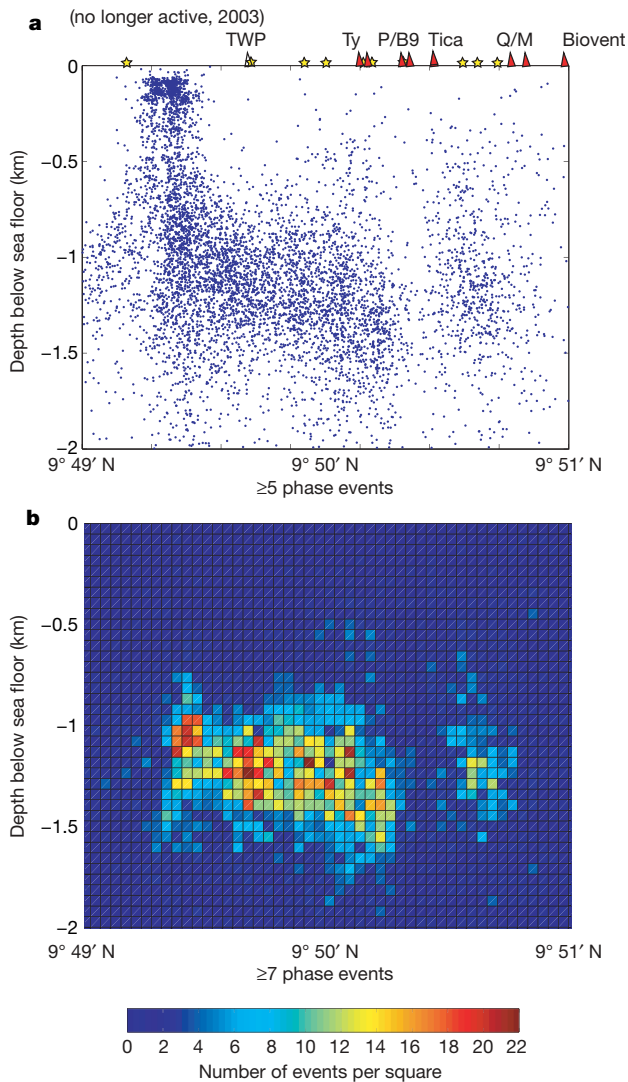

Figure 1 | **Bathymetric site map showing earthquake epicentres. a,** Double-difference epicentre locations (black dots) within the OBS array (blue circles). Also shown are sites of high- and low-temperature venting, margins of the AST (S. A. Soule, personal communication) and imaged AMC[16]. Data include only well-located events (~7,000) with azimuthal gaps ≤180° and more than five defining phase pairs, excluding more poorly located seismic

events outside the array. Dashed box outlines area of Fig. 1b. **b,** Segment end where shoaling pipe seismicity is centred. Shallowest events (cyan dots) show a remarkable fit to the kink along the eastern wall of the AST, and form two distinct groups separated by a gap of a few tens of metres and fanning out at depth. Black asterisk indicates the latitude of the cross-section shown in Fig. 3b.

[1]Lamont-Doherty Earth Observatory of Columbia University, 61 Route 9W, Palisades, New York 10964-8000, USA. †Present address: Marine, Earth and Atmospheric Sciences, Campus Box 8208, North Carolina State University, Raleigh, North Carolina 27695-8208, USA.

Between October 2003 and April 2004, nine two-component (vertical and hydrophone) ocean bottom seismometers (OBSs) were deployed in an array of roughly 4 × 4 km centred at 9° 50′ N on the EPR. Seven continuously recording instruments returned hydrophone data, and six returned vertical-component seismometer data (Fig. 1). Here we present high-resolution double-difference locations for ~7,000 earthquakes that occurred within the array during the 7-month observational period (see Methods Summary). The average relative location error is ~50 m, and the seismicity is closely correlated with geological features identified using high-resolution seafloor imagery and active-source subsurface imaging, implying small absolute errors.

Local event magnitudes within the array range from M_L −1.8 to 1.4, with a magnitude of completeness of roughly M_L −0.5. Detection thresholds were lowest at the southern end of the array near the

highest density of working OBSs, and the minimum magnitude of detectable earthquakes increases with depth because of attenuation. Maximum magnitude also increases with depth above the axial magma chamber (AMC) reflector (~1.43 km)[16] (see Supplementary Fig. 3).

A clearly defined zone of seismicity coincides almost directly with the location and width (~500 m) of the AMC (Fig. 1). The most concentrated band of seismicity, around 200–300 m wide, lies directly underneath the axial summit trough (AST) where the dykes feeding the 1991–92 and the 2006 eruptions were centred[13,15]. This zone lies to the western side of the AMC, suggesting dyke initiation near the chamber's margins where maximum extensional stress concentrations are predicted for pressurized lens-like cavities[17]. The seismic reflection data were collected in 1985, before the 1991–92 eruption, so the AMC may have changed size or location within the 18–19 years before our study. However, the presence of fairly consistent AMC depth at a given spreading rate[18] suggests that its position remains stable between eruptions.

Cross-sections of the hypocentre distribution (Figs 2 and 3) reveal seismicity extending from the upper 100 m to depths of more than 2 km, with a pattern of seismicity that is narrow near the surface and fans out at depth. Within the southern end of the array, the shallowest hypocentres track the eastern wall of the AST (Fig. 1b) and concentrate near a ~100-m kink in the AST. Earthquakes associated with
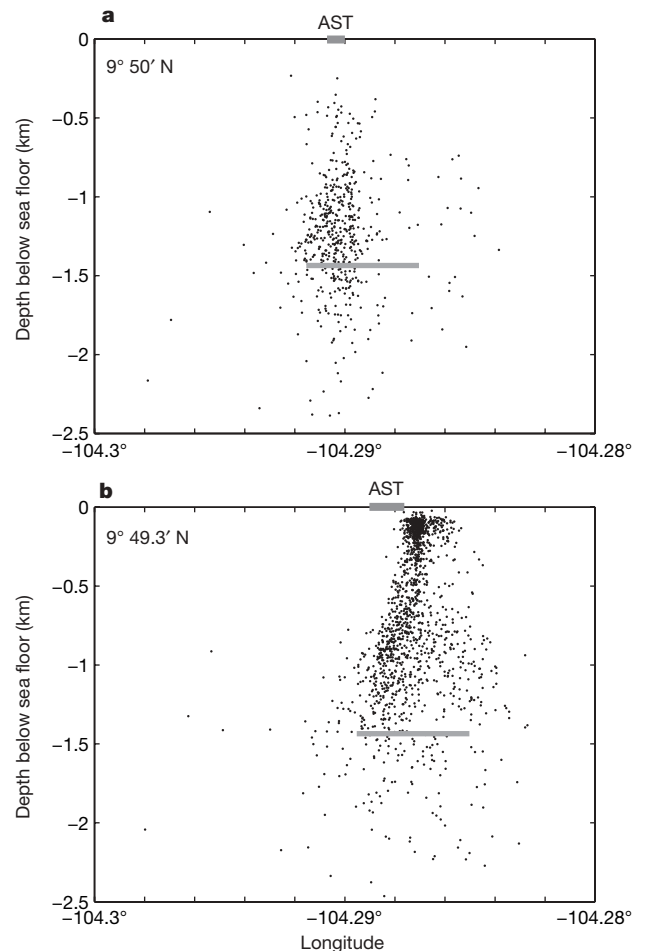
Figure 2 | Along-axis cross-sections of seismicity. a, Events located using five or more seismic phase pairs observed at common stations. Sites of high-temperature (red triangles) and low-temperature (yellow stars) vents are shown. B9 is vent Bio 9; P-vent and Bio 9 are separate but close to each other. Lack of seismicity below TWP (open triangle) is consistent with observations that this former high-temperature vent was inactive in 2003 (ref. 22). **b,** Density plot showing best-recorded events defined by seven or more seismic phase pairs (see also Supplementary Fig. 2). Applying this threshold excludes many of the shallow, small-magnitude events, but reveals a band of seismicity ~500 m thick that deepens to the north. A distinct ~200-m horizontal gap in seismicity is apparent at ~9° 50.3′ N, suggesting a discontinuity within the AMC.

Figure 3 | Across-axis cross-sections of seismicity. Location of the AST is shown in grey box at zero depth. AMC reflector location is marked by grey line at 1.43 km depth[16]. **a,** Profile 200 m wide, centred at 9° 50′ N at the same latitude at which the AMC is imaged in Fig. 1a. **b,** Profile 200 m wide, centred at 9° 49.3′ N across the interpreted down-flow zone (location shown in Fig. 1b). AMC position is inferred from measurements to the north. Seismicity lines up along the eastern AST wall, with a clean edge swooping under the AST with depth, possibly following a bounding fracture surface.

this fourth-order segment boundary[11] form two pipe-like clusters at shallow depth, with the northern cluster fanning out to the north and the southern cluster fanning southward. At depth, the northern cluster has a sharply defined vertical edge suggesting a porosity and/or permeability boundary consistent with crust to the south being slightly older where the kink offsets the southern crustal section ~100 m to the west. We interpret this feature as a hydrothermal down-flow zone, where cold sea water is being entrained into the crust and travelling down to the hydrothermal cracking zone.

This shallowest seismicity at the segment end is likely to be tectonically driven, and its distribution is consistent with the stress field predicted at the tip of a propagating crack[19]. The location 9° 50′ N is the focus of the 1991 and 2006 eruptions, and thus the tips of this segment are more likely to be actively propagating than adjacent segments, perhaps accounting for the dominance of the seismicity on this segment end. This shallow tectonically driven seismicity may form a zone of permeability down which fluids can reach hotter rock where hydrothermal cracking could initiate.

Submersible dives along this 9° 49′ N area of the AST have noted a historic lack of hydrothermal venting and macro-faunal communities (T. Shank, personal communication), supporting the idea that water is going into the crust and not out at this location. Previous studies have suggested that precipitation of anhydrite within the down-flow zone would rapidly clog hydrothermal pathways, requiring a large recharge zone extending across the near-axis flanks in order to maintain hydrothermal systems for decades[9]. The coincidence of this interpreted down-flow zone with an offset in the AST, however, suggests that a high permeability zone may be maintained by stress concentrations within the tip zones of spreading segments[20] and that recharge can be narrowly focused on-axis.

Temporal snapshots show that despite increasing seismicity, the basic structure we image is consistent throughout the 7-month deployment (see Supplementary Fig. 4). Focused down-welling would result in an along-axis thermal gradient that develops through time following an eruption. This prediction is supported by the gradual cooling[21] and eventual cessation of venting at Tube Worm Pillar (TWP)[22], closest to the interpreted down-flow zone, as well as a consistent pattern of heating towards the centre of the segment and cooling towards the ends[21] (see Supplementary Information). Earthquakes recorded during the 22 January 2006 eruption, along with lava effusion rates and plume distribution, suggest that dyking may have initiated in the area 9° 50′ to 9° 50.5′ N (ref. 15). This implies that dyking started where the AMC was least chilled by proximity to down-flow.

An along-axis density plot of the best-recorded (that is, larger magnitude) earthquakes (Fig. 2b) shows a well-defined band of seismicity, around 500 m thick, directly above the AMC. This band is interpreted as a zone of hydrothermal cracking[23,24]. Previous detailed studies of AMC depth on the southern EPR have shown very consistent AMC depths for profiles within 1–2 km of each other, with deepening of the AMC by ~200 m occurring on a length scale of ~100 km(ref. 25). Therefore the slightly sloped pattern of the seismicity cloud is probably due to along-axis thermal trends, or three-dimensional velocity structure that was unaccounted for, rather than short-scale deepening of the AMC along-axis.

The along-axis earthquake distribution shows a sustained ~200-m gap in seismicity around 9° 50.3′ N. This latitude has been associated with differences in the chemistry of diffuse vents at the Bio 9 area versus the Ty/Io and TWP area[26] (Ty and Io are separate but very close chimneys). The gap may thus represent a boundary or transition in the AMC, suggesting segregation of magma at a scale finer than fourth-order discontinuities[11], and perhaps indicating fine-scale transitions from mush to melt as observed in reflection data elsewhere on the EPR[23].

The shoaling of seismicity into a narrower zone underneath the high-temperature vents at 9° 50′ N (Fig. 3a) suggests that the earthquakes in this region may delineate the up-flow area of the circulation
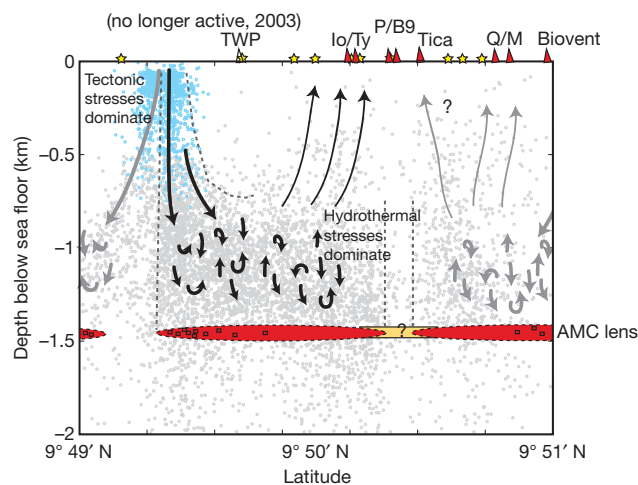
cell. Because of the configuration of the OBS network, shallow events are better resolved beneath the down-flow zone than beneath the active vent area between 9° 50′ N and 9° 51′ N. Consequently, better-defined pipes may exist beneath the up-flow zone.

Our results are not consistent with the shoaling heat source predicted from observations of increasing vent temperatures and changes in fluid chemistry[22]. More than 10 yr of focused up-flow of high-temperature water beneath vents in the 9° 50′ N area may instead have warmed the upper crust and reduced the conductive heat loss. Combined with the likely input of melt into the magma body before the 2006 eruption, this may have helped to fuel the increasing temperatures[21] at the 9° 50′ N focused vents.

Seismicity levels and maximum earthquake magnitude begin to decrease abruptly with increasing depth at ~200 m above the AMC reflector (Supplementary Fig. 3). This may reflect a transition to semi-brittle behaviour with increasing temperature, as well as the potential for greater seismic attenuation along ray paths passing through or near the AMC. Some hypocentres are observed up to a kilometre or more beneath the melt lens, but further work is required to rule out location artefacts.

Notably, we do not detect concentrations of microearthquakes along the flanking margins of the AMC as expected from tomographic models[8] that require significant heat removal on the near-axis flanks. Although we see no evidence for cross-axis circulation or hydrothermal cooling on the flanks, we cannot rule out that it may be happening aseismically or at magnitude levels below our detection capability.

The fact that the across-axis focus is under 500 m wide means that the reservoir volume may be relatively small, which when combined with high heat flow[27] implies that residence times for fluids are likely to be short[6], perhaps less than a year (see Methods). The interpreted hydrothermal cell represents a snapshot in time, and it is likely that

Figure 4 | Cartoon illustrating proposed hydrothermal cell structure. This model shows down-flow at fourth-order discontinuities[11], with the northern vents fed by a down-flow zone at the ~9° 51.5′ N fourth-order discontinuity, and the southern vents fed by the ~9° 49.25′ N offset. The features of the best-defined hydrothermal cell are shown with black arrows, and the features inferred in adjacent cells are shown with grey arrows. Light blue dots illustrate the area where tectonic stresses are likely to dominate earthquake generation, creating a zone of permeability. Light grey dots illustrate where hydrothermal stresses probably dominate. The exact location of this transition is not well constrained. Changes in source from the northern and southern cells may occur between the Ty/Io and the Bio 9 (B9)/P-vent. TWP and Biovent, the closest vents to the inferred down-flow zones, both show decreases in temperature with time, whereas the central vents have been steadily increasing in temperature since about 1994 (ref. 21). Prolonged cooling close to the inferred down-flow zone may lead to a decreasing percentage melt in the AMC. The seismicity gap at ~9° 50.3′ N may represent a break or transition zone (such as melt to mush) within the AMC.

temporal changes in depth, width and intensity occur, with consequences for fluid temperature, chemistry and associated biology. However, microearthquake patterns show no indication of temporal variability in the basic structures they outline, and temperature data support the idea that focused down-flow may be sustained over a decadal timescale at locations of increased tectonic stress (Supplementary Figs 4 and 5). Therefore, it is clear that models showing hydrothermal cells dominantly across-axis may not apply to the fast-spreading EPR. Instead, we interpret flow as narrowly focused along-axis (Fig. 4) on the path of recent dyking where cooling stresses probably result in increased porosity, and heat is most abundant.

METHODS SUMMARY

Analyst-reviewed arrival time picks for P- and S-waves were associated to a total of 16,079 earthquakes in and outside the array. Initial hypocentre locations for a total of 13,911 events recorded by at least four stations were computed using the program *Hypoinverse*[28]. Depth-dependent P- and S-wave velocity models were used to predict travel times and partial derivatives. The velocity models were computed from 476 well-recorded events using the program *Velest*[29]. *Velest* minimizes P- and S-wave travel-time residuals by simultaneous inversion for changes in layer velocities (V_P and V_S), hypocentral parameters, and station corrections.

A total of 35,019 P- and 22,005 S-wave picks were used to locate the 7,362 events that occur within the array of seven stations (azimuthal station gap <180°), and that are presented in this study. On average, the nearest station is 530 m away from each event (horizontally), the farthest station 3 km. Absolute errors computed by *Hypoinverse* have a 1σ median of 0.47 km horizontally and 1.15 km in depth. The root mean square (r.m.s.) of the final travel-time residuals is 32 ms.

We minimize the bias from remaining model errors in the *Hypoinverse* locations by applying the double-difference algorithm *hypoDD*[30] to a total of about 900,000 P- and S-wave differential travel times formed from the phase picks of pairs of events observed at common stations. The algorithm inverts the differential time residuals to solve for the vector connecting the hypocentres. The r.m.s. of the final differential time residuals is 0.010 s, and relative location errors estimated from a bootstrap analysis of the final double-difference vector are 50 m on average.

Full Methods and any associated references are available in the online version of the paper at www.nature.com/nature.

1. Slater, J. G., Jaupart, C. & Glason, D. The heat flow through oceanic and continental crust and the heat loss of the Earth. *Rev. Geophys. Space Phys.* **18**, 269–311 (1980).
2. Stein, C. & Stein, S. Constraints on hydrothermal heat flux through the oceanic lithosphere from global heat flow. *J. Geophys. Res.* **99**, 3081–3095 (1994).
3. Elderfield, H. & Schultz, A. Mid-ocean ridge hydrothermal fluxes and the chemical composition of the ocean. *Annu. Rev. Earth Planet. Sci.* **24**, 191–224 (1996).
4. Lowell, R. P., Rona, P. A. & Von Herzen, R. P. Seafloor hydrothermal systems. *J. Geophys. Res.* **100**, 327–352 (1995).
5. Kelley, D. S., Baross, J. A. & Delaney, J. R. Volcanoes, fluids and life at mid-ocean ridge spreading centers. *Annu. Rev. Earth Planet. Sci.* **30**, 385–491 (2002).
6. Fisher, A. T. in *Energy and Mass Transfer in Marine Hydrothermal Systems* Vol. 3 (eds Halbach, P. E., Tunnicliffe, V. & Hein, J. R.) 29–52 (Dahlem Univ. Press, Berlin, 2003).
7. Johnson, H. P., Becker, K. & Von Herzen, R. Near-axis heat flow measurements on the northern Juan de Fuca Ridge: Implications for fluid circulation in oceanic crust. *Geophys. Res. Lett.* **20**, 1875–1878 (1993).
8. Dunn, R. A., Toomey, D. R. & Solomon, S. C. Three-dimensional seismic structure and physical properties of the crust and shallow mantle beneath the East Pacific Rise at 9°30′ N. *J. Geophys. Res.* **105**, 23537–23555 (2000).
9. Lowell, R. P. & Yao, Y. Anhydrite precipitation and the extent of hydrothermal recharge zones at ocean ridge crests. *J. Geophys. Res.* **107**, doi:10.1029/2001JB001289 (2002).
10. Corliss, J. B. *et al.* Submarine thermal springs on the Galapagos rift. *Science* **203**, 1073–1083 (1979).
11. Haymon, R. M. *et al.* Hydrothermal vent distribution along the East Pacific Rise crest (9°09′–54′ N) and its relationship to magmatic and tectonic processes on fast-spreading mid-ocean ridges. *Earth Planet. Sci. Lett.* **104**, 513–534 (1991).

12. McDuff, R. E. in *Seafloor Hydrothermal Systems* (eds Humphris, S. E., Zierenberg, R. A., Mullineaux, L. S. & Thomson, R. E.) 357–368 (American Geophysical Union, Washington DC, 1995).
13. Haymon, R. M. *et al.* Volcanic eruption of the mid-ocean ridge along the East Pacific Rise crest at 9°45–52′ N: Direct submersible observations of seafloor phenomena associated with an eruption event in April, 1991. *Earth Planet. Sci. Lett.* **119**, 85–101 (1993).
14. Rubin, K., Macdougall, J. D. & Perfit, M. R. 210Po–210Pb dating of recent volcanic eruptions on the sea floor. *Nature* **368**, 841–844 (1994).
15. Tolstoy, M. *et al.* A seafloor spreading event captured by seismometers. *Science* **314**, 1920–1922, doi:0.1126/science.1133950 (2006).
16. Kent, G. M., Harding, A. J. & Orcutt, J. A. Distribution of magma beneath the East Pacific Rise between the Clipperton Transform and the 9° 17′ N deval from forward modelling of common depth point data. *J. Geophys. Res.* **98**, 13971–13995 (1993).
17. Bohnenstiehl, D. R. & Carbotte, S. Faulting patterns near 19°30′ S on the East Pacific Rise: Fault formation and growth at a superfast spreading center. *Geochem. Geophys. Geosyst.* **2**, doi:10.1029/2001GC000156 (2001).
18. Purdy, M., Kong, L. S. L., Christeson, G. L. & Solomon, S. C. Relation between spreading rate and the seismic structure of mid-ocean ridges. *Nature* **355**, 815–817 (1992).
19. Floyd, J. S., Tolstoy, M. & Mutter, J. C. Seismotectonics of mid-ocean ridge propagation in Hess Deep. *Science* **298**, 1765–1768 (2002).
20. Curewitz, D. & Karson, J. A. in *Faulting and Magmatism at Mid-Ocean Ridges* (eds Buck, W. R., Delaney, P. T., Karson, J. A. & Lagabrielle, Y.), Geophysical Monograph 106 117–136 (American Geophysical Union, Washington DC, 1998).
21. Scheirer, D. S., Shank, T. M. & Fornari, D. J. Temperature variations at diffuse and focused flow hydrothermal vent sites along the northern East Pacific Rise. *Geochem. Geophys. Geosyst.* **7**, doi:10.1029/2005GC001094 (2006).
22. Von Damm, K. L. in *Mid-Ocean Ridges: Hydrothermal Interactions between the Lithosphere and Ocean* Geophysical Monograph, **148**, 187–217 (American Geophysical Union, Washington DC, 2004).
23. Singh, S. C., Collier, J. S., Harding, A. J., Kent, G. M. & Orcutt, J. A. Seismic evidence for a hydrothermal layer above the solid roof of the axial magma chamber at the southern East Pacific Rise. *Geology* **27**, 219–222 (1999).
24. Wilcock, W. S. D., Archer, S. D. & Purdy, G. M. Microearthquakes on the Endeavour segment of the Juan de Fuca Ridge. *J. Geophys. Res.* **107**, doi:10.1029/2001JB000505 (2002).
25. Tolstoy, M., Harding, A. J. & Orcutt, J. A. Deepening of the axial magma chamber toward the Garret Fracture Zone from multichannel data. *J. Geophys. Res.* **102**, 3097–3108 (1997).
26. Von Damm, K. L. & Lilley, M. D. in *The Subsurface Biosphere at Mid-Ocean Ridges* Geophysical Monograph 144 245–268 (American Geophysical Union, Washington DC, 2004).
27. Ramondenc, P., Leonid, N. G. A., Von Damm, K. L. & Lowell, R. P. The first measurements of hydrothermal heat output at 9degrees 50′ N, East Pacific Rise. *Earth Planet. Sci. Lett.* **245**, 487–497 (2006).
28. Klein, F. W. User's guide to HYPOINVERSE2000, a Fortran program to solve for earthquake locations and magnitudes. Open-file Report 02–171 (US Geological Survey, 2002).
29. Kissling, E., Ellsworth, W. L., Eberhartphillips, D. & Kradolfer, U. Initial reference models in local earthquake tomography. *J. Geophys. Res.* **99**, 19635–19646 (1994).
30. Waldhauser, F. & Ellsworth, W. L. A double-difference earthquake location algorithm: Method and application to the Northern Hayward Fault, California. *Bull. Seism. Soc. Am.* **90**, 1353–1368 (2000).
31. Vera, E. E. *et al.* The structure of 0- to 0.2-m.y.-old oceanic crust at 9° N on the East Pacific Rise from expanded spread profiles. *J. Geophys. Res.* **95**, 15529–15556 (1990).
32. Harding, A. J., Kent, G. M. & Orcutt, J. A. A multichannel seismic investigation of upper crustal structure at 9° N on the East Pacific Rise: Implications for crustal accretion. *J. Geophys. Res.* **98**, 13925–13944 (1993).
33. Waldhauser, F. HypoDD: A program to compute double-difference hypocenter locations. USGS Open-file Report 01–113 (US Geological Survey, Menlo Park, California, 2001).
34. Bakun, W. H. & Joyner, W. B. The M_L scale in central California. *Bull. Seism. Soc. Am.* **74**, 1827–1843 (1984).

METHODS

Data processing. Velocity information obtained from active source data in our study area[31,32] is used to build a starting model for the *Velest* inversions. The minimum one-dimensional model (Supplementary Fig. 1) fits well with Vera *et al.*[31] Line 7 from ~9° 30′ N. Although this line is 3.1 km off-axis, Harding *et al.*[32] showed that Layer 2A thickens much more rapidly at 9° 50′ N, reaching similar thickness to Line 7 by ~0.5 km off-axis. Therefore Line 7 is the closest comparison to our area, where five of the seven OBSs are 0.5–2 km off-axis.

The double-difference algorithm *hypoDD*[30,33] solves for hypocentral separations by iteratively minimizing residuals between observed and predicted travel-time differences for pairs of earthquakes observed at common stations. Thus, model errors originating from outside the source area are effectively minimized. Given the density of the earthquake distribution, most events are linked to their nearest-neighbour event over distances much smaller than the length scale of the assumed velocity variation sampled by the seismic waves, and thus model errors between each event pair and the stations that recorded both events are virtually cancelled.

The small root mean square value (0.010 s) for the relocated events indicates the consistency of the analyst-refined P- and S-phase arrival time picks produced during the course of this work. The average difference between *Hypoinverse* and *hypoDD* locations is 270 m. We carried out a sensitivity test in which differential travel times were used to confirm the absolute locations produced by *Hypoinverse*. We chose 23 well-recorded events, moved their (*Hypoinverse*) locations south by 1 km and up by 0.3 km, and then used these shifted locations as initial location in a double-difference inversion with P- and S-pick differentials (see ref. 30 for a similar test with synthetic data). In just a few iterations the 23 events moved back to their original *Hypoinverse* locations, demonstrating both the high quality of the phase picks and accuracy of the *Hypoinverse* locations.

Figures 1–3 show event locations in detail for events with five or more phase pairs (Figs 1, 2a and 3). Events with seven or more phase pairs are shown as a density plot in Fig. 2b to highlight the 'cloud' of seismicity that is observed directly overlying the AMC. Supplementary Fig. 2 shows the same events from Fig. 2b as a dot plot.

Supplementary Figs 6 and 7 illustrate how the structure of the interpreted down-welling pipe is constrained by the waveforms, P-arrival time move-out, and S–P move-out.

Magnitudes. Local magnitudes (M_L) were derived using a procedure outlined previously[34] (1984). An empirical distance correction and station correction are applied to the peak displacement amplitude. Supplementary Fig. 3 shows how magnitude varies with depth.

Residence times. Recent heat flow measurements from the high- and low-temperature vent fields at 9° 50′ N suggest that heat flow from all the known vents is ~325 MW (ref. 27). If we assume these vents are fed by two independent but similar-scale hydrothermal cells, then we can divide this heat flow measurement by two to provide an estimate for the heat flow at the hydrothermal cell we image between ~9° 49.25′ N and 9° 59.3′ N, yielding a heat output of ~162.5 MW (1.6×10^8 W).

The dimensions of the hydrothermal cell are ~0.5 km wide and 1.5 km high (conservatively assuming the full upper crust counts for volume) and 1.9 km along-axis. This represents a crustal volume of ~1.42×10^9 m^3 and a fluid reservoir volume (V) of 1.42×10^7 to 1.42×10^8 m^3 for porosities of 1–10%. Residence time (t_r) of fluid within the reservoir is then estimated as:

$$t_r = \frac{V \rho c \Delta T}{H}$$

where ρ (675 kg m^{-3}) and c (6,400 J kg^{-1} K^{-1}) are the fluid density and heat capacity of the fluid, ΔT is the mean temperature difference between the sea floor and reaction zone (350 °C), and H is the observed heat flow. Given the above parameters, $t_r = 4.2$–42 yr, for 1–10% porosity respectively.

If you consider only the ~500-m-thick and ~300-m-wide band of most concentrated seismicity directly overlying the AMC to represent the reservoir, then the reservoir volume at 1% porosity is 2.85×10^6 m^3. Porosity levels are likely to be closer to 1% than 10% considering that this is 'effective porosity' (that is, only pores that are well connected)[6], and that the reservoir seems to be primarily in the lower part of the crust. These assumptions yield a residence time of ~0.8 yr, or about 10 months.